Supporting information

Self-organised shape dynamics of active surfaces

A. Mietke, F. Jülicher, I. F. Sbalzarini

Contents

1 Geometry and mechanics of self-organised active surfaces

In the following, we derive the hydrodynamic equations for the active fluid surface on axisymmetric surfaces, using the general covariant equations introduced in the main text [Eqs. (1)–(4), (10), (11)]. The final equations provide, for a given surface shape and distribution of active tension, a system of partial differential equations for the instantaneous deformation velocity and the meridional in-plane flow. We also present the dynamic equation for the stress-regulator (Eq. (13) in the main text) on axisymmetric surfaces, which is used to evolve the concentration field on the deforming surface.

www.pnas.org/cgi/doi/10.1073/pnas.1810896115

1.1 General parameterisation of an embedded surface

Starting from the general surface parameterisation $\mathbf{X}(s^1, s^2, t)$ introduced in the main text, the Gauss-Weingarten relation [1]

$$\partial_i \mathbf{e}_j = -C_{ij}\mathbf{n} + \Gamma^k_{ij}\mathbf{e}_k \tag{S1}$$

implies for the curvature tensor C_{ij} and Christoffel symbols Γ^k_{ij}

$$C_{ij} = -\mathbf{n}\cdot\partial_i\mathbf{e}_j = \mathbf{e}_j\cdot\partial_i\mathbf{n} \tag{S2}$$

$$\Gamma^k_{ij} = g^{kl}\mathbf{e}_l\cdot\partial_i\mathbf{e}_j = \frac{1}{2}g^{kl}\left(\partial_j g_{il} + \partial_i g_{lj} - \partial_l g_{ij}\right). \tag{S3}$$

The covariant derivative of a tangent vector field $\mathbf{v}_\parallel = v^i\mathbf{e}_i$ and a tensor field $\mathbf{t} = t^{ij}\mathbf{e}_i\otimes\mathbf{e}_j$, where $\otimes$ denotes the dyadic product in $\mathbb{R}^3$, is given by

$$\nabla_i v^j = \mathbf{e}^j\cdot\partial_i\mathbf{v}_\parallel = \partial_i v^j + \Gamma^j_{ik}v^k \tag{S4}$$

$$\nabla_i t^{jk} = \mathbf{e}^j\cdot\partial_i\mathbf{t}\cdot\mathbf{e}^k = \partial_i t^{jk} + \Gamma^j_{il}t^{lk} + \Gamma^k_{il}t^{jl}. \tag{S5}$$

The covariant Levi-Civita tensor is defined by:

$$\mathbf{e}_i\times\mathbf{e}_j = \epsilon_{ij}\mathbf{n}. \tag{S6}$$

1.2 Parameterisation of axisymmetric surfaces

For axisymmetric surfaces, we consider the parameterisation

$$\mathbf{X}(\phi, s, t) = r(s,t)\,\bar{\mathbf{e}}_r + z(s,t)\bar{\mathbf{e}}_z, \tag{S7}$$

where $\bar{\mathbf{e}}_z$ and $\bar{\mathbf{e}}_r$ are the normalised basis vectors of cylindrical coordinates, ϕ is the azimuthal angle and s the arc length parameter. In the following, we determine the explicit form of metric tensor g_{ij}, curvature tensor C_{ij} and Christoffel symbols Γ^k_{ij} using the general definitions introduced above. From here on, we use the coordinates $i\in\{\phi, s\}$ as explicit tensor indices. The basis vectors $\mathbf{e}_i = \partial_i\mathbf{X}$ and $\mathbf{n} = \mathbf{e}_\phi\times\mathbf{e}_s/|\mathbf{e}_\phi\times\mathbf{e}_s|$ read:

$$\mathbf{e}_\phi = \partial_\phi\mathbf{X} = r\bar{\mathbf{e}}_\phi \tag{S8}$$

$$\mathbf{e}_s = \partial_s\mathbf{X} = \partial_s r\,\bar{\mathbf{e}}_r + \partial_s z\,\bar{\mathbf{e}}_z \tag{S9}$$

$$\mathbf{n} = \partial_s z\,\bar{\mathbf{e}}_r - \partial_s r\,\bar{\mathbf{e}}_z. \tag{S10}$$

Using the parameter transformation $h = \partial s(u,t)/\partial u$ between the arc length coordinate s and an Eulerian coordinate u (see Eq. (22) in the main text), the vector $\mathbf{e}_\phi$ is unchanged, and we have $\mathbf{e}_u = h\mathbf{e}_s$. The non-vanishing components of the metric tensor for each parameterisation are therefore given by

$$g_{\phi\phi} = r(s,t)^2 \tag{S11}$$

$$g_{ss} = 1, \tag{S12}$$

and

$$g_{\phi\phi} = r(u,t)^2 \tag{S13}$$

$$g_{uu} := h^2. \tag{S14}$$

Note that Eq. (S12) defines the arc length parameter s and tensor indices 's' can be arbitrarily lifted and lowered, because the metric tensor is diagonal. Using the tangent angle ψ defined by $(\partial_s r, \partial_s z) = (\cos\psi, \sin\psi)$, Eq. (S2) yields the curvature tensor components

$$C^s_{\ s} = C^u_{\ u} = \partial_s \psi(s,t) = \frac{1}{h}\partial_u \psi[s(u,t),t] \tag{S15}$$

$$C^\phi_{\ \phi} = \frac{\sin\psi}{r}. \tag{S16}$$

The Christoffel symbols follow from Eq. (S3) and read:

$$\begin{aligned}\Gamma^\phi_{s\phi} &= \frac{1}{2} g^{\phi\phi}\partial_s g_{\phi\phi} = \frac{\cos\psi}{r} \\ &= \frac{1}{2h} g^{\phi\phi}\partial_u g_{\phi\phi} = \frac{1}{h}\Gamma^\phi_{u\phi}\end{aligned} \tag{S17}$$

$$\begin{aligned}\Gamma^s_{\phi\phi} &= -\frac{1}{2} g^{ss}\partial_s g_{\phi\phi} = -r\cos\psi \\ &= -\frac{1}{2} h^2 g^{uu}\frac{1}{h}\partial_u g_{\phi\phi} = h\Gamma^u_{\phi\phi}.\end{aligned} \tag{S18}$$

The only non-zero Levi-Civita tensor component is

$$\epsilon_{\phi s} = -\epsilon_{s\phi} = r. \tag{S19}$$

1.3 Representation of the governing equations on axisymmetric surfaces

Here, we present the explicit form of the hydrodynamic equations for the active fluid surface, as well as the dynamic equation of the concentration field on axisymmetric surfaces. Note that the final expressions contain the curvature tensor components $C^s_{\ s}$ and $C^\phi_{\ \phi}$, as well as Christoffel symbols $\Gamma^\phi_{\phi s}$. The time evolution of these fields during surface deformations is derived separately in Section 2.1.2.

1.3.1 Hydrodynamic equations for the active fluid film on axisymmetric surfaces

The bending moment tensor $m^H_{ij} = 2\kappa C^k_{\ k}\epsilon_{ij}$ used in this work is purely antisymmetric, such that the normal moment-balance (Eq. (4), main text) with $m^i_n = 0$ implies that the tension tensor has no antisymmetric contribution, i.e. $\epsilon_{ij}t^{ij} = 0$. Using $\epsilon_{ik}\epsilon^{kj} = -\delta^j_i$, the in-plane moment balance (Eq. (3) in the main text) implies:

$$t_{i,n} = 2\kappa\partial_i C^k_{\ k}. \tag{S20}$$

The remaining force balance equations for a surface parameterised by Eq. (S7), read:

$$\partial_s t^s_{\ s} + \Gamma^\phi_{\phi s}\left(t^s_{\ s} - t^\phi_{\ \phi}\right) + C^s_{\ s}t^s_n = -f^{\text{ext}}_s \tag{S21}$$

$$\partial_s t^s_{\ \phi} - \Gamma^s_{\phi\phi}t^\phi_{\ s} + C^\phi_{\ \phi}t^\phi_n = -f^{\text{ext}}_\phi \tag{S22}$$

$$\partial_s t^s_n + \Gamma^\phi_{\phi s}\left(t^s_n + t^\phi_n\right) - C^s_{\ s}t^s_{\ s} - C^\phi_{\ \phi}t^\phi_{\ \phi} = -f^{\text{ext}}_n, \tag{S23}$$

which can be found using Eqs. (S4) and (S5). Here, we have assumed that all fields are axisymmetric, such that they only depend on the arc length parameter s. The components of the tension tensor $t_{ij} = t^d_{ij} + t^H_{ij}$ read

$$t^s_{\ s} = (\eta_s + \eta_b)v^s_{\ s} + (\eta_b - \eta_s)v^\phi_{\ \phi} + \xi f(c) + \gamma + \kappa C^k_{\ k}\left(C^\phi_{\ \phi} - C^s_{\ s}\right) \tag{S24}$$

$$t^{\ \phi}_\phi = (\eta_s + \eta_b)v^\phi_{\ \phi} + (\eta_b - \eta_s)v^s_{\ s} + \xi f(c) + \gamma - \kappa C^k_{\ k}\left(C^\phi_{\ \phi} - C^s_{\ s}\right) \tag{S25}$$

$$t^s_{\ \phi} = r^2 t^{s\phi} = 2\eta_s v^s_{\ \phi}. \tag{S26}$$

The components of the symmetrised strain-rate tensor v_{ij} (Eq. (8), main text) read:

$$v^s{}_s = \partial_s v^s + C^s{}_s v_n \tag{S27}$$

$$v^\phi{}_\phi = \Gamma^\phi_{\phi s} v^s + C^\phi{}_\phi v_n \tag{S28}$$

$$v^s{}_\phi = \frac{r^2}{2}\partial_s v^\phi. \tag{S29}$$

In our examples, we have f^{ext}_ϕ and $t^\phi_n = 0$, such that Eq. (S22) together with Eq. (S29) yields:

$$\partial_s \left(r^2 \partial_s v^\phi\right) + r\cos\psi\, \partial_s v^\phi = 0. \tag{S30}$$

This equation is solved by

$$v^\phi(s) = A\int_0^s \frac{1}{r^3} ds' + v^\phi_0, \tag{S31}$$

with integration constants A and v^ϕ_0. The latter corresponds to rigid-body rotations about the symmetry axis, which appear because we did not include any external friction forces in our description and we can simply choose $v^\phi_0 = 0$. On spherical surfaces, as well as on tubular surfaces with periodic or no-flux boundary conditions, the form of Eq. (S31) implies $A = 0$. Under the assumptions made in this work, Eq. (S22) therefore implies $v^\phi = 0$. Using the explicit form of the tension tensor components of Eqs. (S24) and (S25), the hydrodynamic equations for the active fluid film on axisymmetric surfaces can be obtained from Eqs. (S21) and (S23) and read:

$$(\eta_s + \eta_b)\,\partial_s v^s{}_s + (\eta_b - \eta_s)\,\partial_s v^\phi{}_\phi + 2\eta_s \Gamma^\phi_{\phi s}\left(v^s{}_s - v^\phi{}_\phi\right) + \xi \partial_s f(c) = 0 \tag{S32}$$

$$\begin{aligned}(\eta_s + \eta_b)\left(C^s{}_s v^s{}_s + C^\phi{}_\phi v^\phi{}_\phi\right) + (\eta_b - \eta_s)\left(C^s{}_s v^\phi{}_\phi + C^\phi{}_\phi v^s{}_s\right) + (\xi f(c) + \gamma)\, C^k{}_k \\ -\kappa C^k{}_k \left(C^s{}_s - C^\phi{}_\phi\right)^2 - 2\kappa\left(\partial_s^2 C^k{}_k + \Gamma^\phi_{\phi s}\partial_s C^k{}_k\right) = p.\end{aligned} \tag{S33}$$

Equations (S32) and (S33) form a closed system of ordinary differential equations, which are – for a given geometry – linear in the unknown flow fields v_n, v_s, and in the pressure $f^{\text{ext}}_n = p$.

At the poles of a spherical surface, where $\Gamma^\phi_{\phi s}$ diverges, Eq. (S32) vanishes identically by symmetry, and Eq. (S33) yields a non-trivial analytic limit, which is derived in Section 1.3.3. The following identities are additionally used to avoid the numerical approximation of certain derivatives that appear in those equations:

$$\partial_s C^{\ \phi}_\phi = \Gamma^\phi_{\phi s}\left(C^s{}_s - C^\phi{}_\phi\right)$$

$$\partial_s \Gamma^\phi_{\phi s} = -C^\phi{}_\phi C^s{}_s - (\Gamma^\phi_{\phi s})^2.$$

This directly follows from the explicit form of these fields given in Eqs. (S16) and (S17).

1.3.2 Dynamic equation for the concentration field

The dynamic equation for the concentration field reads:

$$\partial_t c = -\partial_s\left(c v_s\right) - \Gamma^\phi_{s\phi} c v_s - c v_n C^k{}_k + D\left(\partial_s^2 c + \Gamma^\phi_{s\phi}\partial_s c\right) - k\left(c - c_0\right). \tag{S34}$$

1.3.3 Hydrodynamic equations at the poles of axisymmetric spherical surfaces

In the following, we derive expressions for the hydrodynamic Eqs. (S32), (S33) and (S34) at the poles of axisymmetric spherical surfaces, where $r \to 0$ and the Christoffel symbol $\Gamma^{\phi}_{s\phi} = \frac{1}{r}\cos\psi$ diverges. These spurious singularities arise due to the axisymmetric surface parameterisation of a spherical surface. The limits we derive here are used to determine a complete numerical solution of the hydrodynamic balance equations and the dynamic equation for the concentration field, including the points on the poles of spherical surfaces.

From the Taylor theorem, it follows that for any function $g(s) \in C^2(\mathbb{R})$ with $g(u) = 0$

$$\lim_{s\to u} \frac{g(s)}{s-u} = \left.\frac{dg}{ds}\right|_{s=u}. \tag{S35}$$

Furthermore, globally smooth axisymmetric vector fields must vanish at the poles of a spherical surface. This includes the tangential flow v_s, but also derivatives of scalars, such as the mean curvature $H = C^k_{\ k}/2$. With Eq. (S35), we therefore find the limiting values

$$\Gamma^{\phi}_{s\phi} v_s \xrightarrow{s\to 0,L} \partial_s v_s \tag{S36}$$

$$\Gamma^{\phi}_{s\phi} \partial_s C^k_{\ k} \xrightarrow{s\to 0,L} \partial_s^2 C^k_{\ k} \tag{S37}$$

$$\Gamma^{\phi}_{s\phi} \partial_s v_n \xrightarrow{s\to 0,L} \partial_s^2 v_n \tag{S38}$$

at the parametric poles $s = \{0, L\}$. Additionally, the principle curvatures must be equal at the poles, which can be seen by considering $C^{\phi}_{\ \phi} = \frac{1}{r}\sin\psi$ near the pole $s = 0$. There, we have $\psi(s) = \mathcal{O}(s)$ and therefore, using Eq. (18) from the main text,

$$r(s) = \int_0^s \cos\psi(s')ds' = s + \mathcal{O}(s^3). \tag{S39}$$

Using Eq. (S35), we find from Eq. (S16) that

$$\lim_{s\to 0} C^{\phi}_{\ \phi}(s) = \lim_{s\to 0} \frac{\sin\psi}{s} = \partial_s\psi|_{s=0} = C^s_{\ s}|_{s=0}. \tag{S40}$$

Similarly, it can be shown that $C^{\phi}_{\ \phi}|_{s=L} = \partial_s\psi|_{s=L}$ on a spherical surface, such that we indeed have $C^{\phi}_{\ \phi}|_{s=0} = C^s_{\ s}|_{s=0}$ and $C^{\phi}_{\ \phi}|_{s=L} = C^s_{\ s}|_{s=L}$.

Using Eqs. (S36)–(S37), it follows that Eq. (S32) vanishes identically at $s = \{0, L\}$, and Eq. (S33) reads:

$$4\eta_b C^s_{\ s}\left(\partial_s v_s + C^s_{\ s} v_n\right) + 2(\xi f(c) + \gamma)C^s_{\ s} - 8\kappa\partial_s^2 C^s_{\ s} = p \tag{S41}$$

at the poles. This is the final form we use in our numerical scheme to solve the force balance equations at $s = \{0, L\}$.

Using similar arguments, we find for the dynamic equation for the concentration field at the poles of a spherical surface:

$$\partial_t c = 2\left(-\partial_s\left(cv_s\right) - cv_n C^s_{\ s} + D\partial_s^2 c\right) - k\left(c - c_0\right). \tag{S42}$$

2 Dynamic representation of deforming axisymmetric surfaces

Here, we introduce the framework that we have developed to evolve the surface geometry of a deforming axisymmetry surface. First, we derive a set of dynamic equations for the geometric properties that are required to represent the surface implicitly, and to formulate covariant differential equations on the surface. In the second part, we discuss the boundary conditions and additional global constraints that we have considered in this work.

2.1 Dynamic equations for the geometry of deforming axisymmetric surfaces

In the following, we provide the derivations of the dynamic equations for the geometric surface properties. These equations effectively provide a solution for the dynamic equation of the surface $\frac{d}{dt}\mathbf{X} = v_n\mathbf{n}$, where v_n is determined from the hydrodynamic equations introduced in the previous section. An important element of this approach is a time-dependent coordinate transformation, which we derive in the first part of this section. In the second part, we derive the dynamic equations for curvature tensor and Christoffel symbols, which are required to formulate the hydrodynamic equations Eqs. (S32) and (S33) and the dynamic equation of the concentration field Eq. (S34) throughout the deformation process.

2.1.1 Time-dependent coordinate transformation

Consider a dynamic shape change of the surface in a Eulerian parameterisation, such that $\partial_t\mathbf{X} = v_n\mathbf{n}$. Using Eq. (S2), we find:

$$\begin{aligned}\partial_t\mathbf{e}_i &= \partial_i\partial_t\mathbf{X}\\ &= \partial_i\left(v_n\mathbf{n}\right)\\ &= \mathbf{n}\partial_i v_n + v_n C_i{}^j\mathbf{e}_j.\end{aligned} \tag{S43}$$

This implies for the metric tensor

$$\begin{aligned}\partial_t g_{ij} &= 2\mathbf{e}_i\cdot\partial_t\mathbf{e}_j\\ &= 2C_{ij}v_n.\end{aligned} \tag{S44}$$

As explained in the main text, we use in this work a parameter transformation $h(u,t)$ defined by

$$s(u,t) = \int_0^u h(u',t)du', \tag{S45}$$

where u denotes the meridional coordinate of a time-independent Eulerian parameterisation [Eq. (20) in the main text] and s is the arc length coordinate to which u is mapped. With this definition, Eq. (S44) can be used to derive

$$\partial_t h(u,t) = hC^s{}_s v_n, \tag{S46}$$

which represents a dynamic equation for the parameter transformation h.

2.1.2 Dynamic equations of curvature tensor and Christoffel symbols

In the following, we derive the dynamics equations for geometric surface properties. Note that all fields on which partial time derivatives act are evaluated at coordinates of the fixed Eulerian parameterisation. Spatial derivatives with respect to the arc length parameter s are computed using

$$\partial_s = \frac{1}{h}\partial_u. \tag{S47}$$

First, we derive a dynamic equation for the tangent angle ψ. For this, we take the time derivative of both sides of the identity $\sin\psi = \mathbf{e}_u\cdot\bar{\mathbf{e}}_z/h$, which yields

$$\begin{aligned}\cos\psi\partial_t\psi &= \bar{\mathbf{e}}_z\cdot\left(-\mathbf{e}_u\frac{\partial_t h}{h^2} + \frac{1}{h}\partial_t\mathbf{e}_u\right)\\ &= \bar{\mathbf{e}}_z\cdot\left(-\mathbf{e}_s C^s{}_s v_n + \mathbf{n}\partial_s v_n + v_n C^s{}_s\mathbf{e}_s\right)\\ &= \bar{\mathbf{e}}_z\cdot\mathbf{n}\,\partial_s v_n,\end{aligned}$$

where we have used Eq. (S43) to evaluate $\partial_t \mathbf{e}_u$. Using $\bar{\mathbf{e}}_z \cdot \mathbf{n} = -\cos\psi$, we thus obtain

$$\partial_t \psi = -\partial_s v_n. \tag{S48}$$

Although this derivation is only valid for $\psi \neq n + \pi/2$, $n \in \mathbb{Z}$, the same calculation starting with $\cos\psi = \mathbf{e}_u \cdot \bar{\mathbf{e}}_r/h$ shows that Eq. (S48) is indeed valid for all ψ. Using Eqs. (S46) and (S48), we find for the meridional curvature

$$\begin{aligned}
\partial_t C^s{}_s &= \partial_t \left(\frac{1}{h} \partial_u \psi \right) \\
&= -\frac{\partial_t h}{h^2} \partial_u \psi + \partial_s \partial_t \psi \\
&= -C^s{}_s v_n \partial_s \psi - \partial_s^2 v_n \\
&= -(C^s{}_s)^2 v_n - \frac{1}{h} \partial_u \left(\frac{1}{h} \partial_u v_n \right).
\end{aligned} \tag{S49}$$

Similarly, using Eqs. (S16) with (S53), we find for the azimuthal curvature

$$\begin{aligned}
\partial_t C^\phi{}_\phi &= \partial_t \frac{\sin\psi}{r} \\
&= -\frac{\sin\psi}{r^2} \partial_t r + \frac{\cos\psi}{r} \partial_t \psi \\
&= -\left(\frac{\sin\psi}{r} \right)^2 v_n - \frac{\cos\psi}{r} \partial_s v_n \\
&= -(C^\phi{}_\phi)^2 v_n - \frac{1}{h^2} \Gamma^\phi_{\phi u} \partial_u v_n.
\end{aligned} \tag{S50}$$

Note that Eqs. (S49) and (S50) are equivalent at the poles of spherical surfaces, which can be seen from Eq. (S38). Hence, $C^s{}_s = C^\phi{}_\phi$ at the poles remains true during deformations if Eqs. (S49) and (S50) are used to evolve the surface curvature.

For the Christoffel symbol $\Gamma^\phi_{\phi u}$, we have

$$\begin{aligned}
\partial_t \Gamma^\phi_{\phi u} &= \partial_t \left(h \Gamma^\phi_{\phi s} \right) \\
&= v_n C^s{}_s \Gamma^\phi_{\phi u} + h \left(\frac{\sin\psi}{r} \partial_s v_n - \frac{\cos\psi \sin\psi}{r^2} v_n \right) \\
&= v_n C^s{}_s \Gamma^\phi_{\phi u} + C^\phi{}_\phi \partial_u v_n + h v_n \left(\partial_s \frac{\sin\psi}{r} - \frac{\cos\psi}{r} \partial_s \psi \right) \\
&= \partial_u \left(C^\phi{}_\phi v_n \right).
\end{aligned} \tag{S51}$$

In the second step, we have used Eqs. (S17), (S46), (S53), and (S48). In the last two steps we used $\partial_s r = \cos\psi$ and the explicit components of the curvature tensor from Eqs. (S15) and (S16). Similarly, starting with Eq. (S18), we find:

$$\begin{aligned}
\partial_t \Gamma^u_{\phi\phi} &= \partial_t \left(\frac{1}{h} \Gamma^s_{\phi\phi} \right) \\
&= -\frac{v_n C^s{}_s}{h} \Gamma^s_{\phi\phi} - \frac{1}{h} \left(r \sin\psi \partial_s v_n + \cos\psi \sin\psi \, v_n \right) \\
&= -\frac{v_n C^s{}_s}{h} \Gamma^s_{\phi\phi} - \frac{r^2}{h} \left[\frac{\sin\psi}{r} \partial_s v_n - v_n \left(\partial_s \frac{\sin\psi}{r} - \frac{\cos\psi}{r} \partial_s \psi \right) \right] \\
&= \frac{g_{\phi\phi}}{h^2} \left(v_n \partial_u C^\phi{}_\phi - C^\phi{}_\phi \partial_u v_n \right).
\end{aligned} \tag{S52}$$

This relation is not used in the present work but given here for completeness.

2.1.3 Surface reconstruction

As explained in the main text, the axisymmetric surface can be reconstructed by integrating the meridional curvature [Eqs. (17)–(19)]. On spherical surfaces, we integrate the curvature from one surface pole ($s = u = 0$) to the other ($s|_{u=L_0} = L$), where $r(t)|_{u=0} = 0$. The value of $z(t)|_{u=0}$ can be found from integrating $\partial_t z|_{u=0} = -v_n|_{u=0}$. In the following, we show that local constraints at the poles of spherical surfaces are sufficient to ensure that the endpoint of the resulting integral curve remains on the axial symmetry axis. To see this, we use Eq. (S44), which implies $\partial_t g_{\phi\phi}(u,t) = 2g_{\phi\phi}C^{\phi}_{\ \phi}v_n$ and thus:

$$\partial_t r(u,t) = v_n \sin\psi. \tag{S53}$$

Here, we have additionally used Eqs. (S13) and (S16). A surface that is smooth at the poles $s \in \{0, L\}$ obeys $\psi|_{s=0} = 0$ and $\psi|_{s=L} = \pi$. Equation (S53) therefore implies $\partial_t r|_{s=0,L} = 0$, as long as smoothness of the surface at the poles is ensured. The latter is in turn guaranteed by closure conditions on axisymmetric surfaces, which ensure that the deformation field v_n is globally smooth [see Section 2.2.1, Eq. (S56)]. Hence, local constraints are sufficient to ensure $\partial_t r|_{s=0,L} = 0$, such that the endpoint of the reconstructed meridional outline remains on the symmetry axis throughout deformations of the spherical surface.

On periodic tubular surfaces, we use Eqs. (S48) and (S53) to keep track of $\psi(t)|_{u=0}$ and $r(t)|_{u=0}$, respectively. Due to the periodicity of the tubular surface, we can ignore shifts of the point $\mathbf{X}|_{u=0}$ in z-direction and choose for convenience $z(t)|_{u=0} = 0$. Altogether, this allows to reconstruct periodic tubular surfaces using Eqs. (17)–(19) given in the main text.

2.2 Boundary conditions and global constraints for the surface dynamics

Here, we present details on the boundary conditions and global constraints we have used to determine solutions of the hydrodynamic Eqs. (S32), (S33). Fields on axisymmetric spherical surfaces must have specific symmetries at the poles that ensure global smoothness. These *closure conditions* effectively define boundary conditions for solutions of the hydrodynamic equations, which we discuss in the first part of this section. In the second part, we derive a condition on the deformation field v_n that ensures conservation of the volume enclosed by the surface during deformations. The corresponding Lagrange multiplier defines a pressure that we have used as an external force in the numerical solutions. In the last part, we discuss the translational invariance of the hydrodynamic equations and explain how specific reference frames have been chosen in this work to determine unique solutions for the flow field $\mathbf{v}$.

2.2.1 Closure conditions on spherical axisymmetric surfaces

On spherical, axially symmetric surfaces, there exist generic constraints at the parametric poles $s \in \{0, L\}$ that ensure global regularity of the fields and smooth poles throughout the deformation process.

To ensure global smoothness of the field defined on the surface, we require at the poles of an axisymmetric spherical surface

$$\mathbf{v}_{\parallel}\big|_{s=0,L} = 0 \tag{S54}$$

$$\partial_s c|_{s=0,L} = 0. \tag{S55}$$

Smoothness of the surface shape at the poles requires $\psi|_{s=0} = 0$ ($\psi|_{s=L} = \pi$). We see from Eq. (S48) that this is ensured during deformations by the condition

$$\partial_s v_n|_{s=0,L} = 0. \tag{S56}$$

For initial conditions with smooth poles, the constraint Eq. (S56) additionally ensures that the integral representation of a spherical surface is well-defined, which we have discussed in Section 2.1.3.

Equations (S54) and (S56) are formally imposed as boundary conditions when solving the hydrodynamic Eqs. (S32) and (S33) for the in-plane velocity v_s and the deformation velocity v_n on a spherical surface. Eq. (S55) only needs to be fulfilled by the initial condition for c, because on an axisymmetric surface the dynamic equation for the concentration field Eq. (S34) implies $\partial_t(\partial_s c)|_{s=0,L} = 0$.

2.2.2 Conservation of the enclosed volume

We have considered the case where the volume enclosed by the surface is conserved throughout the deformation process. Here, we briefly explain how this constraint was implemented into our framework. The volume enclosed by an axisymmetric surface can be expressed in our parameterisation as

$$V = \pi \int_{z(u_a)}^{z(u_b)} r^2 dz = \pi \int_{u_a}^{u_b} r^2 \sin\psi \, h du. \tag{S57}$$

For a deformation velocity v_n, volume changes are therefore given by

$$\begin{aligned} \partial_t V &= \pi \int_{s(u_a,t)}^{s(u_b,t)} \left(2 r v_n \sin^2\psi - r^2 \cos\psi \, \partial_s v_n + r^2 v_n C^s{}_s \sin\psi\right) ds \\ &= 2\pi \int_{u_a}^{u_b} v_n \sqrt{g} du - \pi r^2 \cos\psi \, v_n\big|_{s(u_a,t)}^{s(u_b,t)} . \end{aligned} \tag{S58}$$

Here, we have used Eqs. (S15), (S46), (S53), and (S48) and $\sqrt{g(u)} = rh$. Equation (S58) is valid for spherical surfaces, as well as for open surfaces ($r|_{s=0}, r|_{s=L} \neq 0$) with $v_s|_{s=0,L} = 0$ and for tubular surfaces with periodic boundary conditions. On spherical surfaces and on tubular surfaces with periodic boundary conditions, the cases studied in this work, the boundary term in Eq. (S58) vanishes. We therefore solve the hydrodynamic Eqs. (S32) and (S33) by additionally imposing

$$\int_{u_a}^{u_b} v_n \sqrt{g} du = 0 \tag{S59}$$

on the deformation velocity v_n. In Eq. (S33), we additionally introduce a homogeneous pressure $p = f_n^{\text{ext}}$ as an external force, which is computed simultaneously with the flow fields v_s and v_n. Note that the pressure effectively serves as the Lagrange multiplier for the constraint Eq. (S59) and ensures that $\partial_t V = 0$.

2.2.3 Translational invariance and choice of reference frame

The hydrodynamic equations describing the active fluid surface are translational invariant, such that solutions are only defined up to a constant velocity vector. In the following, we explain how we eliminated this degeneracy when solving the force balance equations, which requires choosing specific reference frames.

In an axisymmetric parameterisation, only translations along the z-axis with a constant vector $\mathbf{v}_0 = v_0 \bar{\mathbf{e}}_z$ are relevant. In the local basis on the surface such a translation can be expressed as

$$\mathbf{v}_0 = v_0 \left(\sin\psi \, \mathbf{e}_s - \cos\psi \, \mathbf{n}\right). \tag{S60}$$

We denote translation for the purpose of this discussion as $\mathbf{v} = \mathbf{v}' - \mathbf{v}_0$, where $\mathbf{v}'$ and $c'(s',t)$ is an arbitrary solution of the hydrodynamic Eqs. (S32) and (S33) and the dynamic equation of the concentration field Eq. (S34). Using $v_s^0 = v_0 \sin\psi$ and $v_n^0 = -v_0 \cos\psi$, one can verify explicitly that the hydrodynamic equations are unchanged and the dynamic equation of the concentration field is invariant under $\mathbf{v}' \to \mathbf{v} + \mathbf{v}_0$

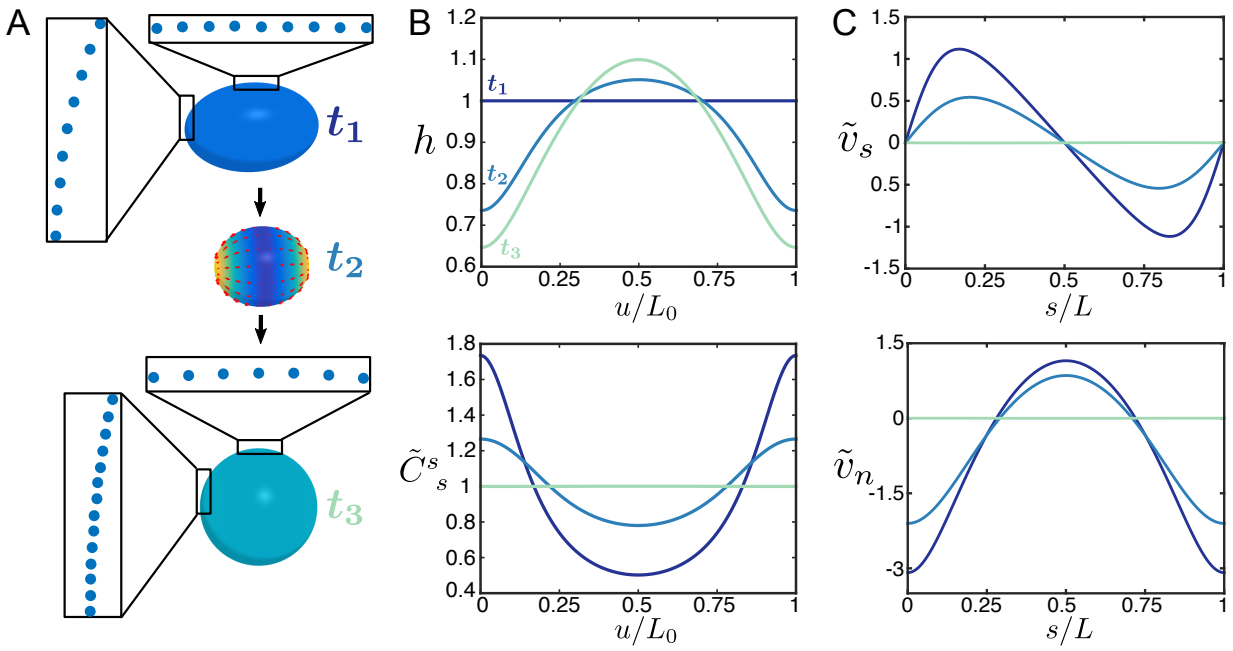

Figure S1: Exemplary dynamics of collocation points and the geometric fields required to reconstruct and iterate the surface shape. *(A)* Collocation points in physical space are initially homogeneously spaced ($h = 1$) and become inhomogeneously distributed during shape changes. *(B)* Coordinate transformation h and dimensionless meridional curvature $\tilde{C}^s{}_s = R_0 C^s{}_s$ in the reference space $\mathcal{S}_0$. Note the compression (dilution) of collocation points in *(A)* in regions with $h < 1$ ($h > 1$). *(C)* In-plane flow field $\tilde{v}_s = v_s\tau/R_0$ and deformation velocity $\tilde{v}_n = v_n\tau/R_0$ ($\tau = \eta_b/\gamma$). The latter is used to determine the temporal changes of the meridional curvature $C^s{}_s$ as explained in the main text.

and $c'(s',t) \to c(s - v_s^0 t, t)$. In the following, we briefly explain which reference frame we have chosen in the different examples shown in the main text and how this fixes v_0 in a way that uniquely defines $\mathbf{v}$.

To fix v_0 on spherical surfaces, we have chosen in this work the reference frame where $\mathbf{v}|_{s=0} = -\mathbf{v}|_{s=L} \Rightarrow v_n|_{s=0} = v_n|_{s=L}$, which implies $v_0 = \left(v_n'|_{s=L} - v_n'|_{s=0}\right)/2$. This choice ensures that $v_n = 0$ everywhere, if the geometry of the surfaces shape is stationary.

On periodic tubular surfaces, it is convenient to impose $\int_0^L v_s ds = 0$ when determining the flow fields using our numerical approach. This choice implicitly fixes $v_0 = \int_0^L v_s' ds/L_0$ and was used for the solutions shown in Figs. 4 B and C. To determine the in-plane flow field in the reference frame of the stationary constriction shown in Fig. 4 D, we have used that the surface geometry does not change in the final steady state. Therefore, the normal flow field must be of the form $v_n' = -v_0' \cos\psi$. We then chose $v_0 = v_0'$, for which $\mathbf{v} = \mathbf{v}' - \mathbf{v}_0$ yields a flow field with $v_n = 0$ and the constriction does not move. The corresponding tangential flow in this reference frame is shown in Fig. 4 D.

3 Details of the numerical approach

In the following, we present a detailed description of the numerical discretisation method we have used to solve the differential equations introduced above. We present validation results of this implementation and list the parameters that used to obtain the numerical solutions presented in this work.

3.1 Numerical discretisation

We discretise Eqs. (S32) and (S33) on the initial arc length domain $\mathcal{S}|_{t=0} = \mathcal{S}_0 = [0, L_0]$ by N equally spaced collocation points. Each point carries the local differential geometric information of the initial shape, given by the extrinsic curvature and the Christoffel symbols, as well as other problem-specific quantities, such as concentration fields. For brevity, we collectively refer to all fields stored on collocation points $u_{(i)} \in \mathcal{S}_0$ as $\{\Phi_{(i)}\}$ (see Fig. 1 B, main text). On this grid, we express the derivative operators of the force balance Eqs. (S32) and (S33) using centred fourth-order finite difference operators [2] and solve the resulting linear system of equations for the flow field components (v_n, $\mathbf{v}_\parallel$) and the internal pressure p using LU decomposition as implemented in Matlab [3]. The latter follows from conservation of the enclosed volume, which is imposed using the integral constraint in Eq. (S58) using Simpson integration weights [2]. Then, we use the dynamic equations for the intrinsic and extrinsic geometry, Eqs. (S46), (S53), and Eqs. (S49)–(S51), as well as the dynamic equation for the concentration field Eq. (S34) to update the set $\{\Phi_{(i)}\}$ using explicit Euler time stepping with step size δt. In subsequent time steps, the coordinate transformation h is used to express all equations in the reference space $\mathcal{S}_0$, which allows solving the force balance equations and evolving the set $\{\Phi_{(i)}\}$ on the same equidistant grid. Figure S1 shows an example of the typical dynamics of collocation points in the physical space, as well as a time series of the different fields that are required to reconstruct and iterate the surface shape. The expected error convergence behaviour $\mathcal{O}(N^{-4}, \delta t)$ is verified in the following section, using a range of numerical tests.

3.2 Grid convergence analysis and simulation code validation

We validate the spatial discretisation of $\mathcal{S}_0$ by solving the hydrodynamic Eqs. (S32) and (S33) for v_s and v_n on a spheroidal surface using increasing numbers N of collocation points. Figure S2 A shows the corresponding behaviour of the maximum error norm with respect to the numerical solution computed for $N = 3201$ collocation points for the flow-field components v_n and v_s, confirming fourth-order convergence.

Next, we validate the temporal convergence using a process as shown in Fig. S1, gradually increasing the number of time steps N_t used to reach a fixed final time point (Fig. S2 B). As expected from using explicit Euler time stepping, the geometric fields converge with $\sim N_t^{-1}$.

Finally, we test the conservation of enclosed volume and total molecule number using a 'numerical experiment' as presented in Fig. 2 C of the main text. The volume is determined by integrating the curvature via Eqs. (17)–(19) and using

$$V = \pi \int_{z(0)}^{z(L)} r^2 dz. \tag{S61}$$

This is an important validation of the constraint imposed by Eq. (S58), which enforces volume conservation using intrinsic fields on the surface, while Eq. (S61) determines the volume using the surface representation in the embedding space. The total amount of the chemical species is given by

$$N_c = \int_\Gamma c \, dA. \tag{S62}$$

Even though the concentration field c and the surface area are changing in space and time in this test case, N_c should be constant when there is no degradation $k = 0$. In this case, only diffusion and advection on the surface, as well as surface-area changes are modulating the local concentration. This validation therefore demonstrates that our reparameterisation approach faithfully evolves the metric properties of the surface. The behaviour of the relative numerical errors for V and N_c over time are depicted in Fig. S2 C.

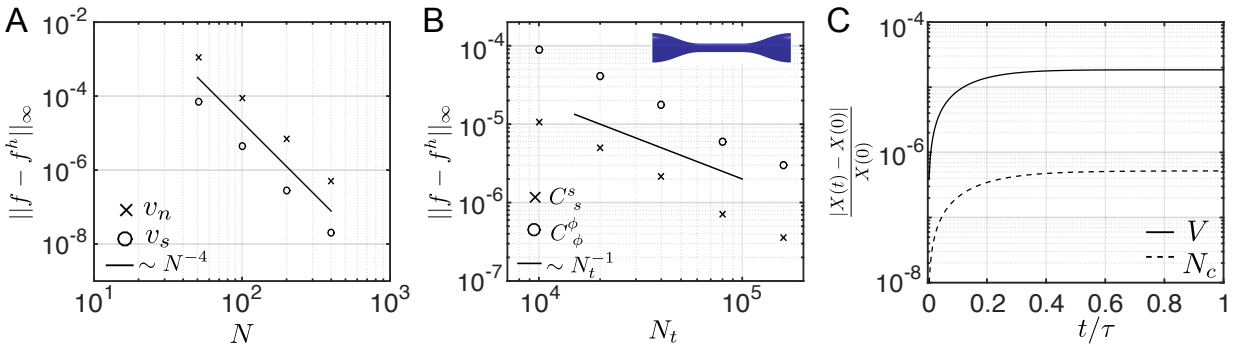

Figure S2: Validation of convergence behaviour and conservation properties. *(A)* Grid convergence of the spatial discretisation: Numerical solutions f^h of Eqs. (S32) and (S33) for single time step on a prolate spheroid with eccentricity 0.6 and homogeneous surface concentration compared with the high-resolution solution f for $N = 3201$ in the maximum error norm $||\cdot||_\infty$. *(B)* Grid convergence of the temporal discretisation: Principle curvatures of a passive tubular surface ($\xi = 0$) after convergence to non-trivial stationary shape (inset) compared with the solution for $N_t = 3.2 \times 10^5$ in the maximum error norm $||\cdot||_\infty$. *(C)* Relative numerical error of the conservation of the enclosed volume and the total amount of the chemical species: Relaxation of an active, spheroidal surface with initial eccentricity 0.6.

3.3 Parameters used for numerical results

	$L_0/(2\pi r_0)$	ξ/γ	$\kappa/(\gamma l_c^2)$	$D\tau/l_c^2$	$k\tau$
Fig. 2 B	–	10	0	0.3	0
Fig. 2 C	–	15	0	8	0
Fig. 3 B	0.95	6	0	0.05	1.95
Fig. 3 C	0.82	6	0	0.05	1.95
Fig. 3 D	1.1	6	0.25	0.05	1.95
Fig. S2 A	–	5	0	–	–
Fig. S2 B	2.5	–	0.15	–	–
Fig. S2 C	–	2	0	4	0

Table S1: Overview of parameters used for the numerical results. The characteristic length for the sphere is its radius $l_c = R_0$, for the tubular surface the radius of the azimuthal cross-section $l_c = r_0$. The characteristic time-scale is given by $\tau = \eta_b/\gamma$. The enclosed volume spherical surfaces was set to $V/R_0^3 = 4\pi/3$. The Hill-coefficient m in Eq. (12) was in all simulations shown in the main text set to $m = 2$, such that $f(c_0) = c_0\partial_c f(c_0) = 1/2$. The surface viscosity ratio was in all simulations set to $\eta_s/\eta_b = 1$.

4 Linear stability analysis

In the following, we present the details of the linear stability analysis from which we have determined the critical contractility parameters α_s^* and α_c^* given in the main text, as well as the stability diagram for a

cylinder surface shown in Fig. 3 A.

4.1 Linear stability analysis of a deforming contractile sphere

We linearise the hydrodynamic equations around the stationary state of a sphere with radius R_0 at rest ($\mathbf{v} = 0$) and a homogeneous concentration field c_0. The internal pressure is given by $p_0^s = 2[\gamma + \xi f(c_0)]/R_0$. We expand perturbations of in-plane flows, shape and concentration as

$$\delta \mathbf{v}_\parallel = \sum_{l=1}^{\infty} \sum_{m \geq -l}^{l} (\delta v_{lm}^{(1)} \mathbf{\Psi}_{lm} + \delta v_{lm}^{(2)} \mathbf{\Phi}_{lm}) \tag{S63}$$

$$\delta R = \sum_{l=0}^{\infty} \sum_{m \geq -l}^{l} \delta R_{lm} Y_{lm} \tag{S64}$$

$$\delta c = \sum_{l=0}^{\infty} \sum_{m \geq -l}^{l} \delta c_{lm} Y_{lm}. \tag{S65}$$

Vector spherical harmonics are defined by [4]

$$\mathbf{\Psi}_{lm} = R_0 \nabla_\Gamma Y_{lm} \tag{S66}$$

$$\mathbf{\Phi}_{lm} = \bar{\mathbf{e}}_R \times \mathbf{\Psi}_{lm}, \tag{S67}$$

where we denote the normalised standard basis of spherical coordinates by $\{\bar{\mathbf{e}}_R, \bar{\mathbf{e}}_\theta, \bar{\mathbf{e}}_\phi\}$. The surface gradient can be written as

$$R_0 \nabla_\Gamma = \bar{\mathbf{e}}_\theta \partial_\theta + \frac{\bar{\mathbf{e}}_\phi}{\sin\theta} \partial_\phi. \tag{S68}$$

Axisymmetry implies $m = 0$ and corresponds to expansion presented in the main text, where $Y_l := Y_{l,m=0}$. However, we note that even if general perturbations are considered the final dispersion relation is independent of m. Volume conservation implies $\delta R_0 = 0$. A homogeneous concentration perturbation with δc_0 simply leads to a change of the internal pressure but does not generate flows and is therefore not relevant for the stability analysis. The modes δR_l with $l \geq 1$, to linear order, do not contribute to changes of the enclosed volume. Therefore, there are no first order contributions to perturbations of the pressure p_0^s for $l \geq 1$. Furthermore, we have to linear order $\delta v_n \approx \delta \dot{R}$, where the dot denotes the derivative with respect to time. With this, the linearisation of the force balance equations and the dynamic equation of the concentration field yields

$$\sum_{l \geq 1} \left(\eta_s (1-l)(2+l) \left(\delta v_l^{(1)} \mathbf{\Psi}_l + \delta v_l^{(2)} \mathbf{\Phi}_l \right) + \left[\eta_b \left(2\delta \dot{R}_l - l(l+1) \delta v_l^{(1)} \right) + R_0 \xi \partial_c f(c_0) \delta c_l \right] \mathbf{\Psi}_l \right) = 0 \tag{S69}$$

$$\sum_{l \geq 1} \left(2\eta_b \left(2\delta \dot{R}_l - l(l+1) \delta v_l^{(1)} \right) + 2R_0 \xi \partial_c f(c_0) \delta c_l + \left(\frac{\kappa}{R_0^2} l(l+1) + \gamma + \xi f(c_0) \right) (l-1)(l+2) \delta R_l \right) Y_l = 0 \tag{S70}$$

$$\sum_{l \geq 1} \left(\delta \dot{c}_l + \frac{c_0}{R_0} \left(2\delta \dot{R}_l - l(l+1) \delta v_l^{(1)} \right) + \left[R_0^2 D l(l+1) + k \right] \delta c_l \right) Y_l = 0. \tag{S71}$$

From the orthogonality of the scalar and vector spherical harmonics it follows that $\delta v_l^{(2)} = 0$ ($l \geq 2$). As there is no friction with the environment, we also have to exclude full body rotations: $\delta v_1^{(2)} = 0$. The $l = 1$ mode yields a pure translation if $\delta \dot{R}_1 = \delta v_1^{(1)}$. However, there is also a surface compression associated with $\delta \dot{R}_1 - \delta v_1^{(1)}$, which tangential and normal force balance relate to the contractility. Together with the dynamic equation of the concentration field, this yields

$$\delta \dot{c}_1 = \left(-\frac{2D}{R_0^2} - k + \frac{\xi}{\eta_b} c_0 \partial_c f(c_0) \right) \delta c_1. \tag{S72}$$

The prefactor in brackets represents the growth rate λ_1 of a perturbation $\delta c_1 = \delta c_{(0)} e^{\lambda_1 t}$ and the definition of the critical contractility parameter α_s^* (Eq. (26), main text) follows from $\lambda_1 = 0$. One can verify that the general Jacobian of this system for $l \geq 2$ yields growth-rates λ_l with $\Re(\lambda_l) < \lambda_1$, such that the polar mode $l = 1$ always becomes unstable first and growth fastest. Note that the bending rigidity κ only contributes to the instability threshold of modes with $l \geq 2$.

4.2 Linear stability analysis of a deforming contractile cylinder

We linearise the hydrodynamic equations around the stationary state of a cylinder surface with radius r_0 and length L_0 at rest ($\mathbf{v} = 0$) and a homogeneous concentration field c_0. The internal pressure is given by $p_0^c = (\gamma + \xi f(c_0) - \kappa r_0^{-2})/r_0$. It follows from Eq. (S9) that, to first order, $\mathbf{e}_s \approx \bar{\mathbf{e}}_z$ and hence $\delta v_s \approx \delta v_z$. We expand perturbations of in-plane flows, shape and concentration as

$$\delta \mathbf{v}_\parallel = \bar{\mathbf{e}}_z \sum_{n=-\infty}^{\infty} \delta v_z^{(n)} \exp(i k_n z) \tag{S73}$$

$$\delta r = \sum_{n=-\infty}^{\infty} \delta r^{(n)} \exp(i k_n z) \tag{S74}$$

$$\delta c = \sum_{n=-\infty}^{\infty} \delta c^{(n)} \exp(i k_n z), \tag{S75}$$

where $k_n = 2\pi n / L_0$. Using these expansions in the hydrodynamic equations yields to linear order:

$$-(\eta_s + \eta_b) k_n^2 \delta v_z^{(n)} + (\eta_b - \eta_s) \frac{i k_n}{r_0} \delta v_n^{(n)} + i k_n \xi \partial_c f(c_0) \delta c^{(n)} = 0 \tag{S76}$$

$$i(\eta_b - \eta_s) \frac{k_n}{r_0} \delta v_z^{(n)} + (\eta_s + \eta_b) \frac{1}{r_0^2} \delta v_n^{(n)} + \frac{\xi}{r_0} \partial_c f(c_0) \delta c^{(n)} + \left[\kappa B_c(k_n r_0) + \frac{\gamma + \xi f(c_0)}{r_0^2} (k_n^2 r_0^2 - 1) \right] \delta r^{(n)} = 0 \tag{S77}$$

$$\partial_t \delta c^{(n)} + c_0 \left(i k_n \delta v_z^{(n)} + \frac{\delta v_n^{(n)}}{r_0} \right) + \left(D k_n^2 + k \right) \delta c^{(n)} = 0, \tag{S78}$$

where we have collected contributions from the bending rigidity into

$$B_c(k_n r_0) = 4 \frac{k_n^2}{r_0^2} + \frac{1}{r_0^4} (2 k_n^2 r_0^2 - 3) \left(k_n^2 r_0^2 - 1 \right). \tag{S79}$$

The function $B_c(k_n r_0)$ describes contributions from deformations of a passive tubular surface with bending rigidity and is equivalent to the results found in Ref [5]. In Eq. (S77), we have also used that shape perturbations $\delta r^{(n)}$ with $|n| \geq 1$ do not change the enclosed volume to linear order, such that no perturbations of the pressure occur to linear for modes with $|n| \geq 1$. Volume conservation additionally implies $\delta r^{(0)} = 0$. Homogeneous perturbations of the concentration field $\delta c^{(0)}$ do not lead to flows and are therefore not relevant for the stability analysis of the shape.

Tangential flows $\delta v_z^{(n)}$ follow from Eqs. (S76) and (S77) as

$$i k_n \delta v_z^{(n)} = \frac{\eta_s - \eta_b}{4 \eta_s \eta_b} \left[-\kappa r_0^2 B_c(k_n r_0) + (\gamma + \xi f(c_0)) \left(1 - k_n^2 r_0^2 \right) \right] \frac{\delta r^{(n)}}{r_0} - \frac{\xi c_0 \partial_c f(c_0)}{2 \eta_b} \frac{\delta c^{(n)}}{c_0},$$

which is used to eliminate $\delta v_z^{(n)}$. Using $\delta v_n \approx \delta \dot{r}$ to first order, we find the linearised, closed dynamical system in $(\delta r^{(n)}, \delta c^{(n)})$ given by

$$\frac{\partial_t \delta r^{(n)}}{r_0} = \frac{\eta_s + \eta_b}{4\eta_s \eta_b} \left[-\kappa r_0^2 B_c(k_n r_0) + (\gamma + \xi f(c_0)) \left(1 - k_n^2 r_0^2\right) \right] \frac{\delta r^{(n)}}{r_0} - \frac{\xi c_0 \partial_c f(c_0)}{2\eta_b} \frac{\delta c^{(n)}}{c_0} \tag{S80}$$

$$\frac{\partial_t \delta c^{(n)}}{c_0} = \frac{1}{2\eta_b} \left[\kappa r_0^2 B_c(k_n r_0) - (\gamma + \xi f(c_0)) \left(1 - k_n^2 r_0^2\right) \right] \frac{\delta r^{(n)}}{r_0} + \left(\frac{\xi c_0 \partial_c f(c_0)}{\eta_b} - D k_n^2 - k \right) \frac{\delta c^{(n)}}{c_0}. \tag{S81}$$

Equations (S80) and (S81) define a Jacobian $\underline{\mathbf{J}}(k_n)$ for each mode n by:

$$\begin{pmatrix} \partial_t \delta r^{(n)}/r_0 \\ \partial_t \delta c^{(n)}/c_0 \end{pmatrix} = \underline{\mathbf{J}}(k_n) \cdot \begin{pmatrix} \delta r^{(n)}/r_0 \\ \delta c^{(n)}/c_0 \end{pmatrix}. \tag{S82}$$

The eigenvalues of $\underline{\mathbf{J}}(k_n)$ have been determined numerically to construct the stability diagram shown in Fig. 3 A. For a passive tubular surface ($\xi = 0$) without bending rigidity ($\kappa = 0$) the growth-rate of shape perturbations is positive for

$$\left(1 - k_n^2 r_0^2\right) > 0 \Leftrightarrow L > 2\pi r_0. \tag{S83}$$

This corresponds to the classical Plateau-Rayleigh instability that is only determined by the geometry of the cylinder.

In the following, we present a brief analytic characterisation of $\underline{\mathbf{J}}$ near the critical contractility α_c^* given in Eq. (27) (main text) for $\kappa = 0$. Note that $\underline{\mathbf{J}}(k_n) = \underline{\mathbf{J}}(-k_n)$, such that we restrict the following discussion to $k_n \geq 0$. For the purpose of this analysis, we introduce a dimensionless wavenumber $\tilde{k}_n := k_n r_0$, such that the Plateau-Rayleigh threshold is $\tilde{k}_n = 1$, and a viscosity parameter $\bar{\nu} = (\eta_s + \eta_b)(4\eta_s) > 1/4$.

The stationary state is stable if and only if $\mathrm{Tr}(\underline{\mathbf{J}}) < 0$ and $\det(\underline{\mathbf{J}}) > 0$ [6]. The condition $\mathrm{Tr}(\underline{\mathbf{J}}) = 0$ defines the critical wavenumber

$$\tilde{k}_n^c = \sqrt{\frac{\alpha\gamma - \eta_b k + \bar{\nu}[\gamma + \xi f(c_0)]}{\eta_b D/r_0^2 + \bar{\nu}[\gamma + \xi f(c_0)]}}, \tag{S84}$$

and $\mathrm{Tr}(\underline{\mathbf{J}}) > 0$ ($\mathrm{Tr}(\underline{\mathbf{J}}) < 0$) for $\tilde{k}_n < \tilde{k}_n^c$ ($\tilde{k}_n > \tilde{k}_n^c$). The point $\tilde{k}_n^c = 1$ then defines the critical contractility α_c^* given in Eq. (27) (main text) and shown as black dashed line in Fig. 3 A. Furthermore, $\alpha > \alpha_c^*$ ($\alpha < \alpha_c^*$) implies $\tilde{k}_n^c > 1$ ($\tilde{k}_n^c < 1$). Hence, if $\alpha > \alpha_c^*$ then there must exist a $\tilde{k}_n > 1$ with $\mathrm{Tr}(\underline{\mathbf{J}}) > 0$, such that the relative length L_0/r_0 at which unstable cylinders exist, is reduced compared to the length given by the Plateau-Rayleigh criterion in Eq. (S83). This corresponds to the decrease in the aspect ratio at which the cylinder becomes unstable when α becomes larger than α_c^*.

To characterise this point further, we consider the positive roots of $\det(\underline{\mathbf{J}}) = 0$ and $\kappa = 0$ given by:

$$\tilde{k}_n^{(1)} = 1 \tag{S85}$$

$$\tilde{k}_n^{(2)} = \sqrt{\frac{\alpha\gamma - (\eta_b + \eta_s)k}{(\eta_b + \eta_s)D/r_0^2}}. \tag{S86}$$

From this, we see that $\alpha < \alpha_c^*$ implies $\tilde{k}_n^{(2)} < 1$, as well as $\tilde{k}_n^{(2)} < \tilde{k}_n^c < 1$. From the analysis of the determinant it follows furthermore that $\tilde{k}_n^{(2)} < 1$ implies $\det(\underline{\mathbf{J}}) > 0$ for $\tilde{k}_n > 1$ and $\det(\underline{\mathbf{J}}) < 0$ for $\tilde{k}_n^{(2)} < \tilde{k}_n < 1$. If $\alpha < \alpha_c^*$, cylinders are therefore stable for $\tilde{k}_n > 1$ ($\mathrm{Tr}(\underline{\mathbf{J}}) < 0$, $\det(\underline{\mathbf{J}}) > 0$) and unstable for $\tilde{k}_n < 1$, which amounts to the Plateau-Rayleigh criterion in Eq. (S83).

To conclude, we have demonstrated that, for $\alpha < \alpha_c^*$, active cylindrical surfaces essentially behave like a passive tube, the stability of which is only affected by the geometric Plateau-Rayleigh criterion. Above the contractility threshold, $\alpha > \alpha_c^*$, the mechano-chemical self-organisation of the surface starts to interfere with this behaviour, leading to a reduction in the maximum aspect ratio at which cylindrical surfaces are stable.

References

[1] Erwin Kreyszig. *Introduction to differential geometry and Riemannian geometry.* University of Toronto Press, 1968.

[2] C. Pozrikidis. *Numerical Computation in Science and Engineering.* Oxford University Press, 1998.

[3] Matlab 2015b. The MathWorks, Natick, MA, USA.

[4] Rubén G. Barrera, G. A. Estevez, and J. Giraldo. Vector spherical harmonics and their application to magnetostatics. *Eur. J. Phys.*, 6(4):287–294, 1985.

[5] Ou-Yang Zhong-can and Wolfgang Helfrich. Bending energy of vesicle membranes: General expressions for the first, second, and third variation of the shape energy and applications to spheres and cylinders. *Phys. Rev. A*, 39:5280–5288, 1989.

[6] Michael Cross and Henry Greenside. *Pattern Formation and Dynamics in Nonequilibrium Systems.* Cambridge University Press, Cambridge, 2009.

SI Video Captions

SI Video 1: Spontaneous formation of contractility pattern and surface shape with polar asymmetry. Red arrows denote the in-plane flow field $\mathbf{v}_\parallel$. Colours represent the concentration of stress-regulator (see Fig. 2 B for colour code). The characteristic time is defined as $\tau = \eta_b/\gamma$. Parameters: $V/R_0^3 = 4\pi/3$, $\xi/\gamma = 10$, $D\tau/R_0^2 = 0.3$, $\eta_s/\eta_b = 1$, Hill-coefficient in $f(c)$ (Eq. 12): $m = 2$.

SI Video 2: Shape relaxation. Red arrows denote the in-plane flow field $\mathbf{v}_\parallel$. Colours represent the concentration of stress-regulator (see Fig. 2 C for colour code). The characteristic time is defined as $\tau = \eta_b/\gamma$. Parameters: $V/R_0^3 = 4\pi/3$, $\xi/\gamma = 15$, $D\tau/R_0^2 = 8$, $\eta_s/\eta_b = 1$, Hill-coefficient in $f(c)$ (Eq. 12): $m = 2$.

SI Video 3: Self-organised constriction of a tubular surface. Red arrows denote the in-plane flow field $\mathbf{v}_\parallel$. Colours represent the concentration of stress-regulator (see Fig. 3 B for colour code). The characteristic time is defined as $\tau = \eta_b/\gamma$. Parameters: $L_0/(2\pi r_0) = 0.95$, $\xi/\gamma = 6$, $D\tau/R_0^2 = 0.05$, $\eta_s/\eta_b = 1$, Hill-coefficient in $f(c)$ (Eq. 12): $m = 2$, $k\tau = 1.95$.

SI Video 4: Mechano-chemical shape oscillation of a tubular surface. Red arrows denote the in-plane flow field $\mathbf{v}_\parallel$. Colours represent the concentration of stress-regulator (see Fig. 3 C for colour code). The characteristic time is defined as $\tau = \eta_b/\gamma$. Parameters: $L_0/(2\pi r_0) = 0.82$, $\xi/\gamma = 6$, $D\tau/R_0^2 = 0.05$, $\eta_s/\eta_b = 1$, Hill-coefficient in $f(c)$ (Eq. 12): $m = 2$, $k\tau = 1.95$.

SI Video 5: Spontaneous symmetry breaking and peristaltic motion of a tubular surface with bending rigidity. Red arrows denote the in-plane flow field $\mathbf{v}_\parallel$. The shape dynamics is shown in the reference frame where $\int_0^L v_s ds = 0$. Colours represent the concentration of stress-regulator (see Fig. 3 B for colour code). The characteristic time is defined as $\tau = \eta_b/\gamma$. Parameters: $L_0/(2\pi r_0) = 1.1$, $\xi/\gamma = 6$, $D\tau/R_0^2 = 0.05$, $\eta_s/\eta_b = 1$, Hill-coefficient in $f(c)$ (Eq. 12): $m = 2$, $k\tau = 1.95$, $\kappa/(\gamma r_0^2) = 0.25$.